

Structure and Infrastructure Engineering



Maintenance, Management, Life-Cycle Design and Performance

ISSN: (Print) (Online) Journal homepage: https://www.tandfonline.com/loi/nsie20

Uncertainty quantification in digital image correlation for experimental evaluation of deep learning based damage diagnostic

Nur Sila Gulgec , Martin Takáč & Shamim N. Pakzad

To cite this article: Nur Sila Gulgec , Martin Takáč & Shamim N. Pakzad (2020): Uncertainty quantification in digital image correlation for experimental evaluation of deep learning based damage diagnostic, Structure and Infrastructure Engineering, DOI: 10.1080/15732479.2020.1815224

To link to this article: https://doi.org/10.1080/15732479.2020.1815224

	Published online: 09 Sep 2020.
	Submit your article to this journal 🗷
ılıl	Article views: 106
Q ^L	View related articles 🗷
CrossMark	View Crossmark data ☑





Uncertainty quantification in digital image correlation for experimental evaluation of deep learning based damage diagnostic

Nur Sila Gulgec^a, Martin Takáč^b and Shamim N. Pakzad^a

^aDepartment of Civil and Environmental Engineering, Lehigh University, Bethlehem, PA, USA; ^bDepartment of Industrial and System Engineering, Lehigh University, Bethlehem, PA, USA

ABSTRACT

As the temporal and spatial resolution of monitoring data drastically increases by advances in sensing technology, structural health monitoring applications reach the thresholds of big data. Deep neural networks are ideally suited to use large representative training datasets to learn complex damage features. One such real-time deep learning platform that was developed to solve damage detection and localisation challenge in the authors previous paper. This network was trained by using simulated structural connection with a variety of loading cases, damage scenarios, and measurement noise levels for robust diagnosis of damage. In this article, this platform is validated by using the data collected by Digital Image Correlation (DIC) which offers a non-contact method to measure full-field strain by increasing the flexibility of their implementation. Nevertheless, the capabilities of DIC while measuring small strain responses is limited. This article first investigates the accuracy of the strain measurements of a structural component subjected to operational loads which are often smaller than 50 μ E. The accuracy of three DIC systems with different camera resolutions is compared with the measurements collected by strain gauges and finite element model. Then, the performance and efficiency of damage diagnosis approach is evaluated on two induced damage conditions.

ARTICLE HISTORY

Received 25 December 2019 Revised 16 June 2020 Accepted 28 June 2020

KEYWORDS

Structural health monitoring; damage detection; deep learning; convolutional neural networks; digital image correlation; uncertainty; strain measurement

1. Introduction

Structural systems are subjected to deterioration and damage during their service life due to environmental and operational factors. Providing timely damage assessment becomes essential to improve lifetime safety, maintainability and reliability of the structures and infrastructure systems. Therefore, structural health monitoring (SHM) techniques have been developed to inform engineers about the variations of the structures over their entire lifespan from the collected sensor measurements (Fang, Luo, & Tang, 2005).

Strain response has been widely collected because they are a direct indicator of stress, and can be used to assess failure (Gulgec, Takáč, & Pakzad, 2017, 2020). Nevertheless, the change in the strains does not occur only because of the deterioration; for instance, strain gradients are often observable near connections, or when material exceeds its elastic limit. With the increase in the scale and complexity of the specimen, determining the cause of these variations require manual effort and experience. The authors previously proposed a natural way of exploring the hidden knowledge in raw strain field data by adopting deep learning-based approach in Gulgec, Takáč, and Pakzad (2019a). Learning such damage features helps automatising the detection procedure and provides easy adaption to the varying loading and environmental conditions.

Wire strain gauges are one of the most widely used strain measurement tools in SHM (Kim et al., 2007). Nevertheless, large scale deployment of wired strain gauges poses several fundamental limitations: they are laborious and expensive as more spatial information is desired, as well as they are susceptible to drift and damages (Gulgec, Takáč, & Pakzad, 2019b). To address these limitations, digital image correlation (DIC) was introduced in the early 1980s as a non-contact sensing method which utilises the greyscale digital images captured during the loading of the specimen and performs image processing techniques to estimate the fullfield deformation of the object without the need of attaching to the structure (Sutton, Wolters, Peters, Ranson, & McNeill, 1983). Since then, many studies have been proposed to explore the potential of DIC as a feasible alternative to wire strain gauges for obtaining full-field strain measurement in the laboratory and the field (Pan, 2018).

The DIC technique has been used to measure micro to large amplitude strains due to its easy deployment. Nevertheless, in practice, there are many factors that impact the measurement accuracy of DIC (Amiot et al., 2013; Haddadi & Belhabib, 2008; Reu, 2011; Siebert, Becker, Spiltthof, Neumann, & Krupka, 2007). The systematic errors caused by the shape functions (Schreier, Braasch, & Sutton, 2000), intensity interpolation (Bing, Hui-Min, Bo-Qin, & Fu-Long, 2006; Hung & Voloshin, 2003), lens distortion (Yoneyama, Kikuta, Kitagawa, & Kitamura, 2006; Zhang,

Luo, & Arola, 2006), subset size (Bornert et al., 2009), the speckle pattern (Crammond, Boyd, & Dulieu-Barton, 2013; Lecompte et al., 2006), out-of-lane motion (Sutton, Yan, Tiwari, Schreier, & Orteu, 2008), the contrast of the image (Yaofeng & Pang, 2007), and the quality of devices (Patterson et al., 2007) have been thoroughly investigated in the literature. Furthermore, several studies demonstrated that camera systems should be corrected for temperature when there is a wide temperature fluctuations (Mehdi Mirzazadeh & Green, 2018). For instance, average strain errors vary 70–230 $\mu \epsilon$ when camera temperature changes by 9–14 °C (Ma, Pang, & Ma, 2012).

Literature has demonstrated promising results with DIC while measuring medium-large strain levels (Berfield et al., 2007; Grytten, Daiyan, Polanco-Loria, & Dumoulin, 2009; Jerabek, Major, & Lang, 2010; Lagattu, Bridier, Villechaise, & Brillaud, 2006; Pritchard, Lava, Debruyne, & Terentjev, 2013; Wang et al., 2010). However, non-negligible errors have been observed when measuring strains below 0.1% (1000 με) (Chu, Ranson, & Sutton, 1985; Hung & Voloshin, 2003; Lee, Take, & Hoult, 2012; Périé, Calloch, Cluzel, & Hild, 2002). Several studies reported various standard deviations of the strain readings (i.e. noise floor) which are 50 µE (Haddadi & Belhabib, 2008), 100 με (Smith, Li, & Tong, 1998), 200 με (Wattrisse, Chrysochoos, Muracciole, & Némoz-Gaillard, 2001) and 1000 με (Risbet, Feissel, Roland, Brancherie, & Roelandt, 2010) depending on specific experimental and equipment conditions. The reported deviations are the amplitudes which are often observable in structures under the operational load levels (Alampalli & Lund, 2006; Tennyson, Mufti, Rizkalla, Tadros, & Benmokrane, 2001). There are also several studies that searched for the capabilities of DIC measuring strain readings smaller than 100 με (Acciaioli, Lionello, & Baleani, 2018; Desai, 2016; Dinh, Hassan, Dyskin, & MacNish, 2015; Hutt & Cawley, 2009; Pan, Xie, Wang, Qian, & Wang, 2008) for only small-scale specimens. Therefore, the investigation of accurate full-field strain information of large-scale structural components is still a necessity to discover the current capabilities of DIC.

One of the primary purposes of this study is to explore whether small strain responses (i.e. strain values smaller than 50 $\mu\epsilon$) are achievable with the current DIC systems and to present some recommended techniques for achieving that. To accomplish this goal, a steel structural connection introduced in Gulgec et al. (2019a) is tested on a controlled laboratory environment by using three DIC systems with different camera resolutions. The accuracy of dense strain readings is compared with the measurements collected by strain gauges and finite element model mimicking the specimen. The effect of camera resolution is also discussed.

After the investigation of the accuracy of DIC measurements, this article evaluates the proposed deep learning based damage diagnosis platform introduced in Gulgec et al. (2019a) by using the collected data from the specimen. Laboratory testing of the specimen mimicking the simulated structural connection is performed with two induced damage conditions. The network parameters from the designed

network are utilised to quantify the uncertainty existing in the three DIC systems.

The rest of the article is organised as follows. First, an overview of the proposed methodology is described in Section 2; then, a brief explanation of related work and the basic principles of DIC are provided in Section 3. In Section 4, test setup is described. Then, the analysis of data and experimental validation of the test setup are presented in Section 5 and Section 6, respectively. Conclusions and future directions are given in Section 7.

2. Overview of the proposed methodolgy

Convolutional neural networks (CNN) are one of the most widely used types of deep neural networks which was first proposed by LeCun et al. in 1998 (LeCun, Bottou, Bengio, & Haffner, 1998) to classify handwritten digits. CNNs are designed to take advantage of the spatial correlation of data and can be constructed by using three types of layers: convolution (CONV) layer, pooling (POOL) layer and fully-connected (FC) layer.

The adopted CNN-based technique proposed in Gulgec et al. (2019a) is briefly discussed in this section. More detailed information can be found in the provided reference. As presented in Figure 1, a general map of the algorithm is composed of training and testing phases. Training phase operates on the strain fields obtained from finite element simulations which is then normalised by its absolute maximum. The design of the CNN architecture depends on the selection of hyperparameters (e.g. the number of CONV layers, learning rate, and many more). Once the network architecture is built by these hyperparameters, it is trained to determine the existence of damage (i.e. detection task) and estimate the boundaries of the damaged area (i.e. localisation task). Both of the tasks share layers to extract local features which are common for them. This provides more efficient learning, shorter training time and lower computa-

The network architecture consists of three convolutional layers followed by two task-specific fully connected layers. The convolutional layers receive the input layer and pass them through a filter size of 3×3 . The network forms 8, 16 and 32 feature maps after these convolutional layers. The max-pooling operation, which has the size of 2×2 with a stride of 2, performs right after first and second convolution layer. The feature maps of the last convolutional layer are stacked together in an array and employed as an input to the task-specific layers. The FC layer sizes for the detection task are [836-767], whereas they are [2058-881-534] for the localisation task. The learning rate of 0.0451 and 0.0026 are adopted for the detection and localisation parts, respectively.

Trained parameters are saved to test the performance of strain field collected by digital image correlation system. In this phase, raw strain fields collected from DIC are fed into the proposed architecture to estimate the labels for detection and localisation tasks.

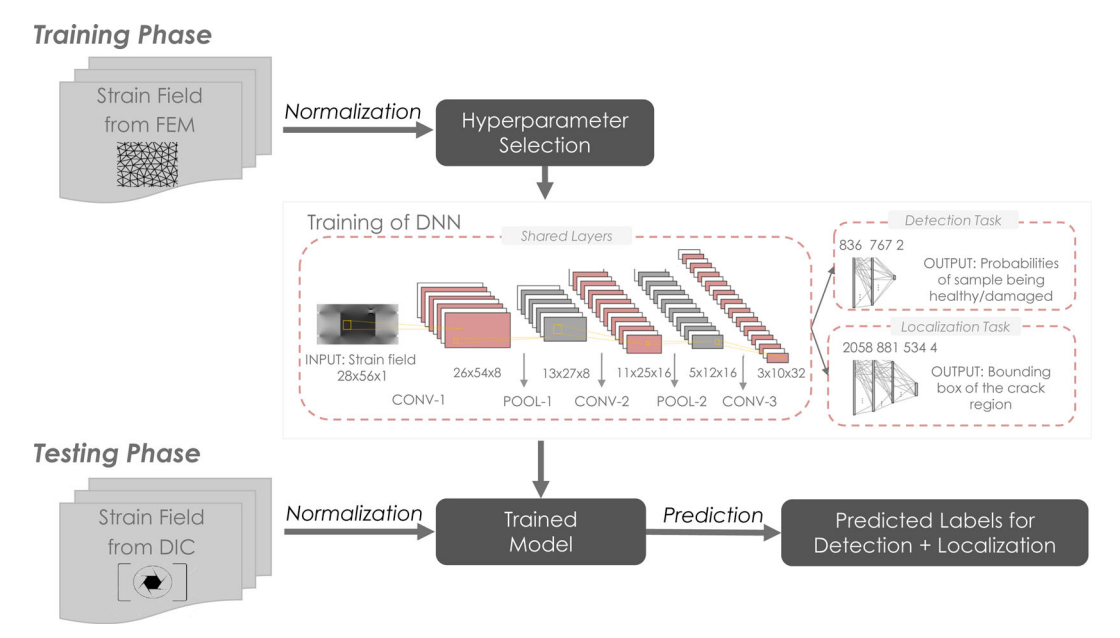


Figure 1. Proposed framework for damage diagnosis.

3. Background on digital image correlation

Digital image correlation techniques aim to measure the deformations of the specimen from the images taken by digital cameras. Cameras first capture a reference image in an original unloaded state. They continue taking more pictures as the specimen deforms (Desai, 2016). The reference area in the image, which is called the region of interest (ROI), is divided into square image fragments (i.e. subsets or facets) which have a unique grey-scale pattern of pixels (Figure 2). Each subset needs to be distinct enough to facilitate matching; therefore, the test specimen surface needs to have random gray intensities and deform with the specimen with the loading. The subsets in the reference and other images are matched with the facet matching process (Pan, Xie, & Wang, 2010). Such procedure finds the maximum similarity between the deformed subset centred at point P'(x', y') and reference subset centred at P(x, y). Similarity can be found by using different subpixel interpolations, e.g. bilinear interpolation, bicubic interpolation and spline interpolation (GOM, 2013). After the matching process of all subsets in the images, the displacement field computed based on the centre points of the subsets. Strain values are determined by calculating the gradients of the displacement.

3.1. Overview of three-dimensional digital image correlation

The matching process of 3D-DIC consists of two steps: stereo and temporal matching (Tang, Liang, Xiao, & Guo, 2012). The stereo tracking requires matching of the subsets in the images taken by the left and right cameras; whereas, temporal matching aims to track the subsets in the reference and deformed images captured by the same camera as in 2D-DIC (Pan et al., 2008). After the matching of all subsets in the images, 3D coordinates of all the points are obtained through a triangulation method. Triangulation utilises the

information obtained from sensor calibration to determine the spatial coordinates of the corresponding image points (Pan et al., 2010). During calibration, several images are captured from different angles and focal lengths of the specimen to track the rotations and translations.

The 3D displacement of the subsets in each stage can be obtained simply by comparing its 3D coordinates in the deformed stage and the reference stage after the 3D reconstruction of all the stages (GOM, 2013). The strains are computed tangential to the surface by measuring the elongation of neighbour point coordinates (LeBlanc, Niezrecki, Avitabile, Chen, & Sherwood, 2013). The deformation gradient tensor can be calculated by using at least three points which form triangles. The density of the selected points differs from region to region. The weighting factor can be employed to choose the involved points and determine their distance to the centre of the surface (GOM, 2013).

4. Experimental setup

A series of tests of a steel structural connection was conducted in the structural laboratory to evaluate the performance of the DIC systems when measuring small strains and quantifying the uncertainty in DIC for damage diagnostic. The tests were performed by using three different camera systems under two different damage scenarios.

The test setup including the specimen, GOM Aramis 3D DIC system, and external light sources (i.e. dual Blue LED attached to the DIC camera bars and high intensity LED light kit) are illustrated in Figure 3a. The tensile loads were applied by using the SATEC 2670 kN (600kip) Hydraulic Testing System at the end of connections with an eccentricity to obtain axial force and bending moment at the connection. During the loading process, strains were measured with the DIC technique on the front face of the specimen as well as with the strain gauges on the back surface. Then,

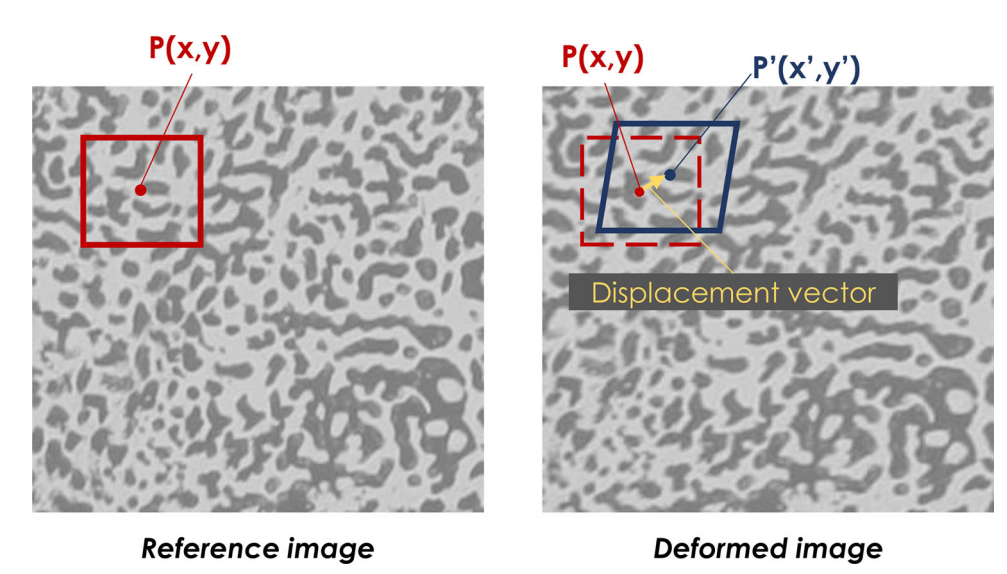


Figure 2. Principle of DIC.

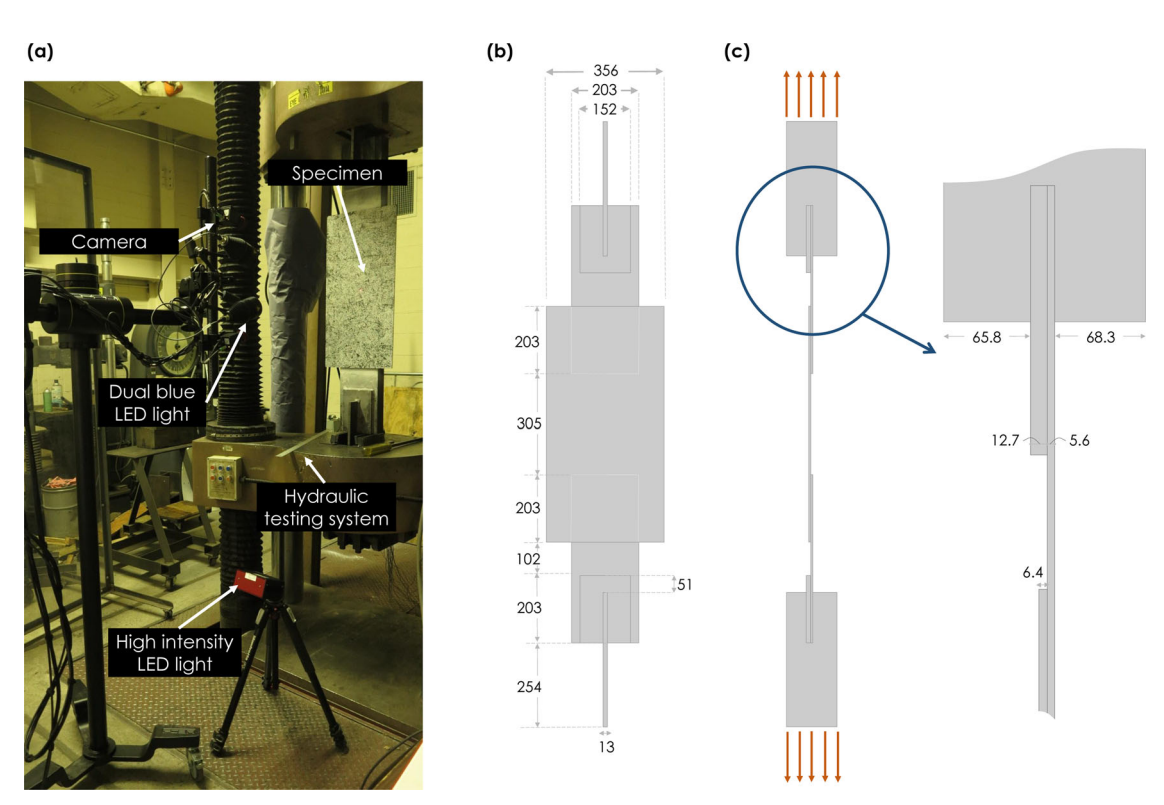


Figure 3. (a) Test setup, (b) Dimensions of the steel connection, (c) Side view of the specimen (all units in mm).

both of these methods were compared with the finite element model mimicking the specimen.

4.1. Description of the specimen

The tested specimen is composed of two 508 mm-long C200 \times 17.1 (mm \times kg/m) (i.e. C8 \times 11.5 (in. \times lb/ft)) channels welded to a steel plate with a dimension of 711 \times 356 \times 6 mm (28 \times 14 \times 1/4 inches) where all members are made of steel with a yield strength of 250 MPa. Each channel member has a 203 mm overlap with the main gusset plate. The dimensions of the steel connection and its side

view are visualised in Figure 3b and c. The load was applied at the ends of the specimen with the help of the steel plate in the direction of the grips of the hydraulic testing system. Dense strain measurements of the specimen were collected during different stages of loading.

In order to track the changes in the gray-scale, a random pattern was applied on the front surface of the specimen. The background of the pattern was generated by spraying white paint with primer; then, black speckles are randomly spread with a rubber stamp. A closer look at the pattern is presented in Figure 4a. The average dot size of 1.5 mm was obtained to have an optimum speckle size of 3–5 pixels (Schreier, Orteu, & Sutton, 2009). The black to white area

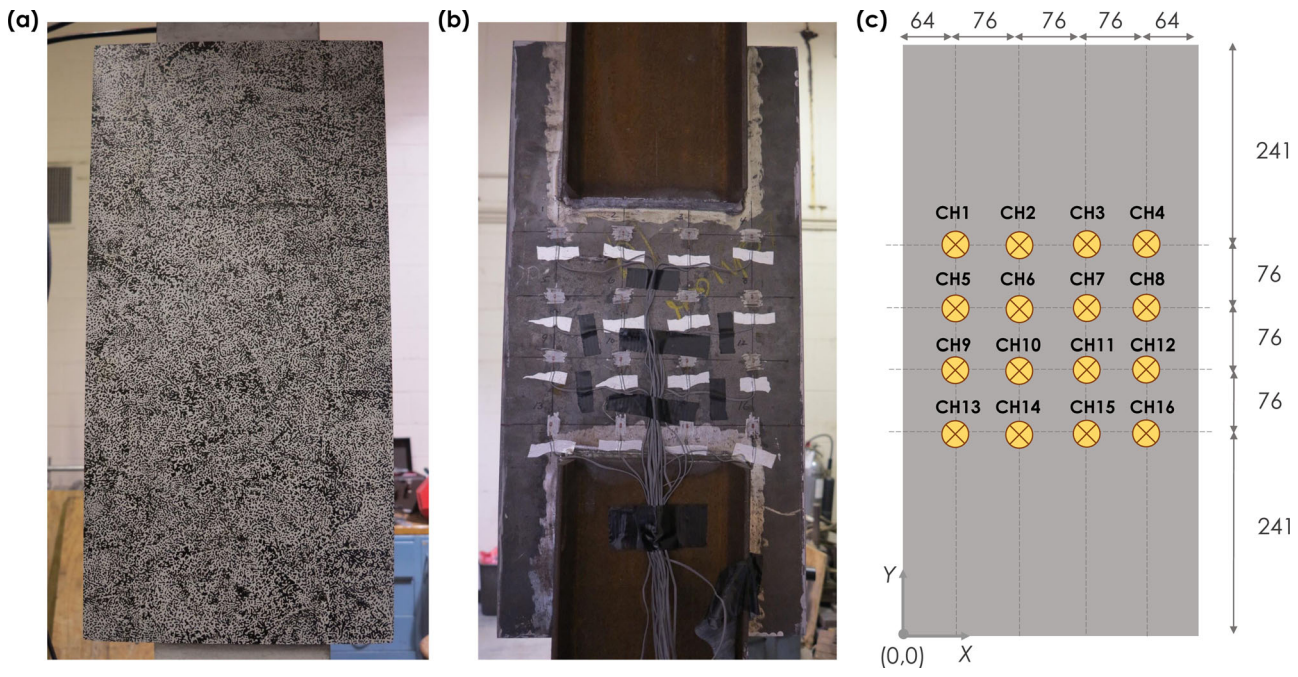


Figure 4. (a) The pattern applied on the front surface, (b) Installed strain gauges, (c) The strain gauge locations on the back surface (all units in mm).

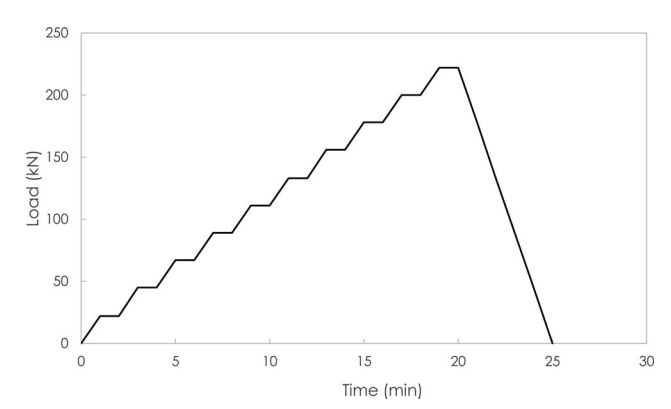


Figure 5. Loading Scheme.

ratio of the pattern was approximately 50%-50% which is the desired ratio in common practice (Berfield et al., 2007).

On the back surface of the plate, sixteen FLA-1-11-1LJC type, 1 mm bondable strain gauges were installed which are manufactured by Tokyo Sokki Kenkyujo Co., Ltd. Gauge factor of 2.14 is utilised (Figure 4b). These gauges (CH1-CH16) were attached to the steel at the locations shown in Figure 4c.

4.2. Loading of the specimen

The test was conducted within the linear elastic range of the material behaviour. The plate was gradually loaded to 222 kN (50 kips) and unloaded to its zero-load position. The quasistatic loading scheme is presented in Figure 5. After every 22 kN (5 kips) load increment, the load was held for a minute to allow DIC to take pictures. For each constant load, 200 pictures were acquired with the sampling rate of 4 Hz. The strain gauge readings were collected with a frequency of 2 Hz.

4.3. DIC procedure

Digital images of the specimen were captured by using three different 3D DIC systems (Aramis Adjustable 2.3 M, 6 M and 12 M, GOM mbH where M stands for Megapixel). Table 1 summarises the system properties of the three optical systems. Schneider high precision lenses with a focal length of 24 mm were used with 12 M system, whereas Kowa LM12HC-V 1" c-mount lenses are used for 2.3 M and 6 M cameras. Cameras were mounted onto rigid support integrated to rugged studio stand. The angle between the cameras was adjusted to 25 degrees based on the manufacturer's recommendations. Similar measurement volumes were obtained for each system by adopting different camera-specimen and camera-camera distances. Measurement volumes were selected such that they capture the full steel plate volume $(711 \times 356 \times 6 \,\mathrm{mm})$. In order to eliminate the error due to self-heating, the cameras were preheated for 1-2 hours before the DIC experiment (Ma et al., 2012).

3D calibration was carried out before each test-session by using a coded panel with a size of 356 mm by 279 mm. After the calibration, rigid support and cameras were rotated vertically to take advantage of the camera resolution. To get consistent illumination, dual Blue LED attached to the DIC camera bars with mounting arms and high intensity LED light kit was used as an external lighting source. These light sources were utilised to illuminate the specimen and balance the effect of the ambient light existing in the laboratory. To achieve more stable pictures, exposure time was set less than 50 ms.

4.4. Damage scenarios

Cracks were ground in the coordinates which were not used in the training data shown as black lines in Figure 6. Two damage scenarios were considered in the assessment of the

Table 1. DIC system properties.

	Aramis 2.3 M	Aramis 6 M	Aramis 12 M		
Camera resolution	1936 × 1216 pixel	2752 × 2200 pixel	4096 × 3068 pixel		
Maximum frame rate	130 Hz	25 Hz	335 Hz		
Lense brand and size	Kowa, 12.5 mm	Kowa, 12.5 mm	Schneider, 24 mm		
Camera-specimen distance	930 mm	902 mm	890 mm		
Camera-camera distance	380 mm	361 mm	366 mm		
Measurement volume	760/510/510 mm	800/690/690 mm	790/640/640 mm		

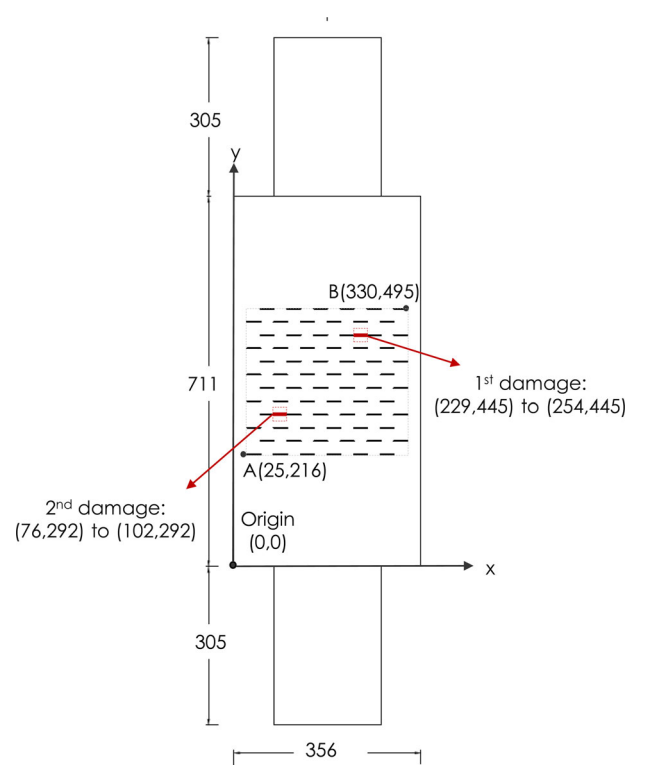


Figure 6. Crack locations (all units in mm).

methodology. First scenario included only the first crack location in the coordinates (229,445) to (254,445). The first crack location was defined by the bounding box of (229,445, 254,470). In the second case study, another crack in the coordinates (76,292) to (102,292) was ground to have evolving crack scenario. The bounding box of this crack location was defined as (76,292, 102,318).

4.5. Preparation of FE model

The finite element model, which mimics the test setup, was simulated in Abaqus 6.14 by using shell elements. The material was modelled as elastic-perfectly plastic with a yield strength of 250 MPa. Mesh size of 13 mm was adopted. Damage was introduced as 26 mm long crack with the seam option of the software and solved by the Newton method. The welded connections were modelled as tie constraints (Garifullin, Bronzova, Jokinen, Heinisuo, & Kovačič, 2016). The distributed loads were applied to the end of the channels to simulate the constant loads shown in Figure 4a (e.g. 1.5 kN/mm for 222 kN). The other end is simulated as encastre. Strain distribution in the direction of loading (ϵ_y) was utilised where an example strain distribution is visualised in Figure 7.

5. Analysis of data

Digital images of the test object are subsequently processed by using ARAMIS Professional 2017 software (GOM, 2013). The software evaluates high-resolution images recorded from the specimen during loading, then automatically computes 3D coordinates for all loading stages and derives strain results. The post-processing algorithm of software has a stage-wise analysis, in which each stage consisted of one image.

In this study, the reference image is selected as the first image taken under the load of 22 kN. The same reference load level is also utilised while measuring with strain gauges. The strain field (ϵ_y) in the direction of the loading is computed. In order to reduce the noise floor and achieve higher accuracy while measuring small strain values, a baseline is constructed with the average of all images captured during the 22 kN loading stage. The calculated baseline is subtracted from all images.

The subset size is an important factor in DIC data analysis. The increase in the subset size results in a lower error but higher computation cost. On the other hand, a smaller step size yields more points and provides higher spatial resolution (Crammond et al., 2013) which causes a trade-off between using large and small subset sizes. Several studies have investigated how the subset size should be selected. Sutton, Orteu, and Schreier (2009) suggests that subset size should contain at least three speckles such that there is a distinctive pattern in the subset. The subset size of 21×21 pixels is recommended as a minimum practical size by the study referred in Reu (2012).

Another critical factor in DIC computations is the spacing between the subset centres (i.e. step size). The step size can be chosen such that subsets partially overlap with the neighbour subsets. A common practice recommends a step size of one-third to one-half of the subset size (Jones & Iadicola, 2018). In this study, the subset size of 40 with a step size of 20 is used while analysing 12 M and 6 M DIC systems. For the 2 M system, the subset size is selected as 22 with a step size of 11. Although filtering reduces the noise and increases accuracy, it also reduces the spatial resolution (GOM, 2013). Therefore, no spatial filtering is performed during the analysis. Instead, a feature of Aramis software called strain neighbourhood size is utilised where the strain is computed from a weighted average of the involved points. The size of five is adopted to smooth the measurements without losing most of their spatial content.

Computed strain fields of the stages from each ten load levels $\{22\,kN,\,45\,kN,\,\ldots,\,222\,kN\}$ is shown in Figure 8. The axis of the colorbar is set to $[-200,\,1000]~\mu\text{m/m}$ for all stages to illustrate the effect of the crack on the axial strain.

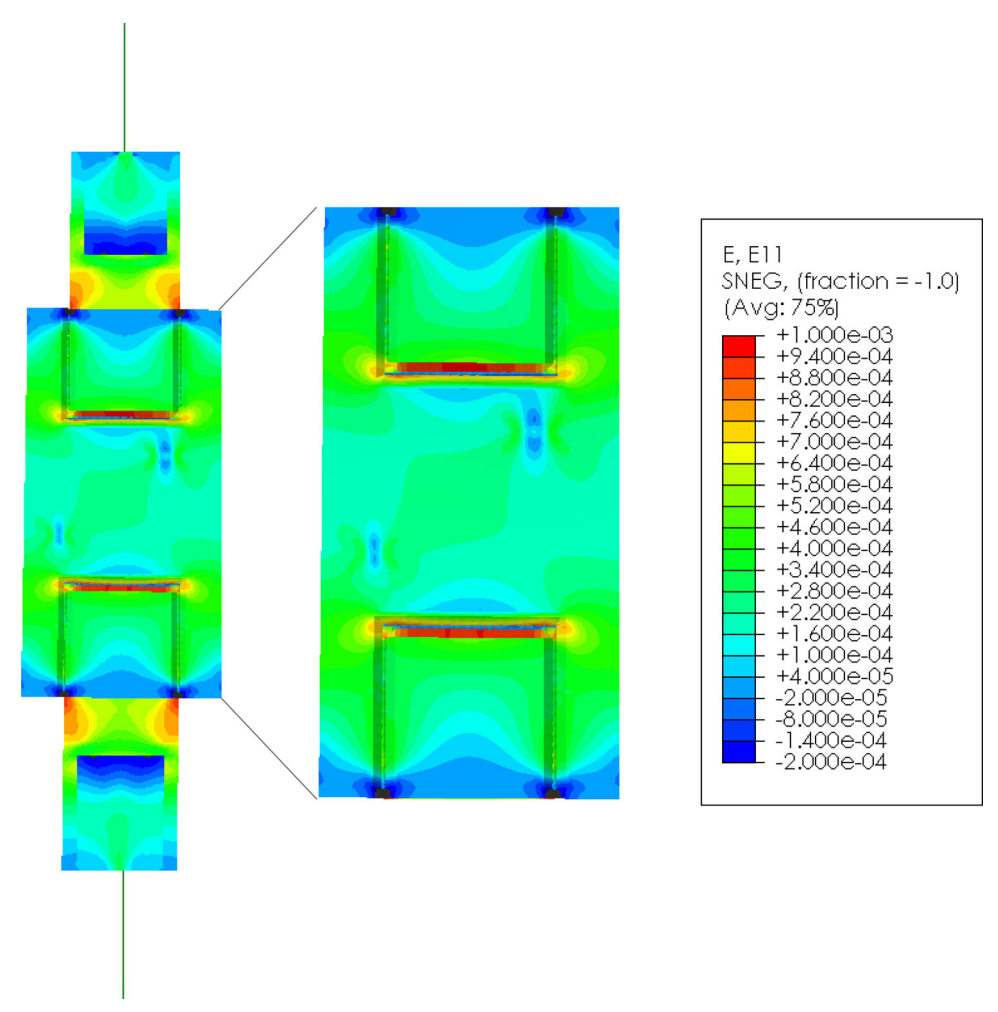


Figure 7. FE model of the plate under 200 kN.

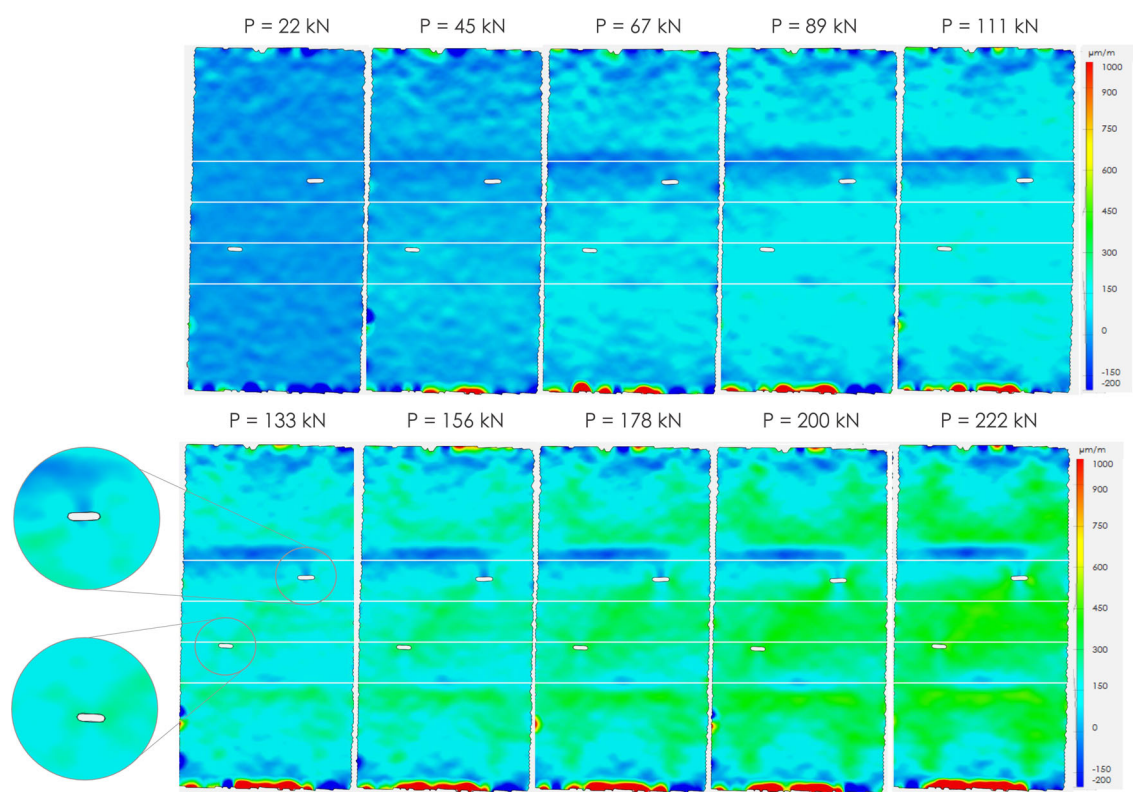


Figure 8. Strain fields.

It is noticeable that strain gradients start to occur near the crack tips when the load is greater than 133 kN. Another observation is the development of the negative strains, especially near the section where plate is welded to the top channel member. Such behaviour might be relevant to the loading of the specimen given that only the top grip of the hydraulic system moves. The potential small downward movement of the top grip might cause a push at the top end of the specimen during the holding of the load.

In order to better analyse the results, the strain measurement obtained from several cross-sections (i.e. Plane Y = 241 mm, Y = 317 mm, Y = 393 mm, Y = 469 mm) are visualised in Figure 9 for the first damage scenario and Figure 10 for the second damage scenario. In the figures, each line represents averaged strain measurements per each load level for three different camera resolutions. Due to the linear loading pattern, the strains should increase linearly in a similar trend with each consecutive loading. In other words, the difference of the measurements at 222 kN (50 kips) and 200 kN (45 kips) should be the same as the measurements at 200 kN and 178 kN when material behaviour is within its linear range. The strain curves of Figure 9 show that strains increase linearly in a similar trend with each consecutive loading for the 12 M DIC system. The only exception is observed for the sections Y = 241 mm and Y = 469 mm.

Another observation that strain measurements smaller than $50\mu\epsilon$ are successfully achieved. Nevertheless, similar accuracy is not accomplished for 6 M and 2.3 M systems. Although the trend and amplitudes match the ones measured by the 12 M system, the difference between consecutive loads is not clear in lower resolution cameras. Similar conclusions can be drawn for the second damage scenario shown in Figure 10. In the plots, the gradient change due to the second crack can be easily observed in the cross-section Plane Y=317 mm from X=50 to 150 mm.

In order to characterise the degree of linearity quantitatively, the statistics of the difference between each consecutive load is presented with the cross-section plots. The fourth column of Figures 9 and 10 shows the mean (μ) and standard deviation (σ) pairs of the differences for each consecutive loading pairs. The tables show that the difference in means and the standard deviation of the differences are approximately $5\mu\epsilon$ and $7\mu\epsilon$ for 12 M DIC system, respectively. The standard deviation of the differences and the fluctuations in the mean increase with the reduction in the resolution.

The assessment of the performance of the sensors includes the comparison of DIC systems and strain gauges with the FE model for the front and back side of the specimen, respectively. This evaluation method is preferred due to the eccentricity in the loading and asymmetry in the specimen. This section first compares the DIC measurements with the FE model, then discusses the performance of strain gauges for the first crack scenario.

5.1. Digital image correlation - FEM comparison

Figures 11–14 show the comparison between the strains measured using DIC systems and FE analysis. The specimen is

loaded within its elastic range of response. For this reason, the normalised strain readings should give similar behaviour for each consecutive loading. For each loading except the reference load of 22 kN, stages are normalised by the load level. Then, the trajectories of the normalised strain readings are plotted in red with their averages. This step is repeated for three DIC systems with different resolutions as described earlier. Similarly, strain measurements from the FE model are normalised by the load level and plotted in the same figures in blue.

Figures show that FE and DIC measurements have similar trends, especially closer to the crack location which can be seen on the curves given in Figures 11 and 12. Additionally, the better match between FEM and DIC is observable with the increase in the resolution of the cameras. 2.3 M system introduces more uncertainty to the system and causes more deviations in the measurements. The largest difference between strain/load measured by FE and DIC is observed in Figure 11 because of the negative strains developed on the Y = 469 mm. Although FE model captures this compressive behaviour in the section (Figure 7), the strains computed through FEA are higher than the test setup. The difference might be due to the specimen alignment during the testing since even a small deviation in the alignment may intensify the compressive strains in the section $Y = 469 \,\mathrm{mm}$. Another high variation between the FE and DIC strains is seen from X=0 to 75 mm and from X = 275 to 350 in Figure 14. It is because the section Y = 241 mm is close to Y = 203 mm where the cross section changes (i.e. the cross section change is shown in Figure 3).

5.2. Strain gauge - FEM comparison

Figures 15–18 show the comparison between the strains measured using strain gauges versus FE simulation. For each loading except the reference load of 22 kN, gauge readings are averaged together and normalised by the load level. Then, the boxplots of the normalised strain readings are plotted in red. This step is repeated for the tests performed while testing three DIC systems with different resolutions. The strains from FE model are also normalised by the load level and plotted in the same figures in blue. Figures show that trend and amplitude of the strain gauges often match well with FE results except for the sections Y = 241 mm and Y = 469 mm. These sections are close to the region between the gusset plate and channel members. Therefore, the reasoning explained in Section 5.1 applies to strain gauge – FEM comparison as well.

6. Experimental evaluation of the methodology

Full-field measurement data obtained by DIC was analysed in Section 5. This section evaluates the performance of the trained network on data collected from DIC for detection and localisation tasks.

6.1. Detection results

The DIC data is sampled from every 13 mm to have the mesh size as adopted in the FE model; thus, the strain fields with a

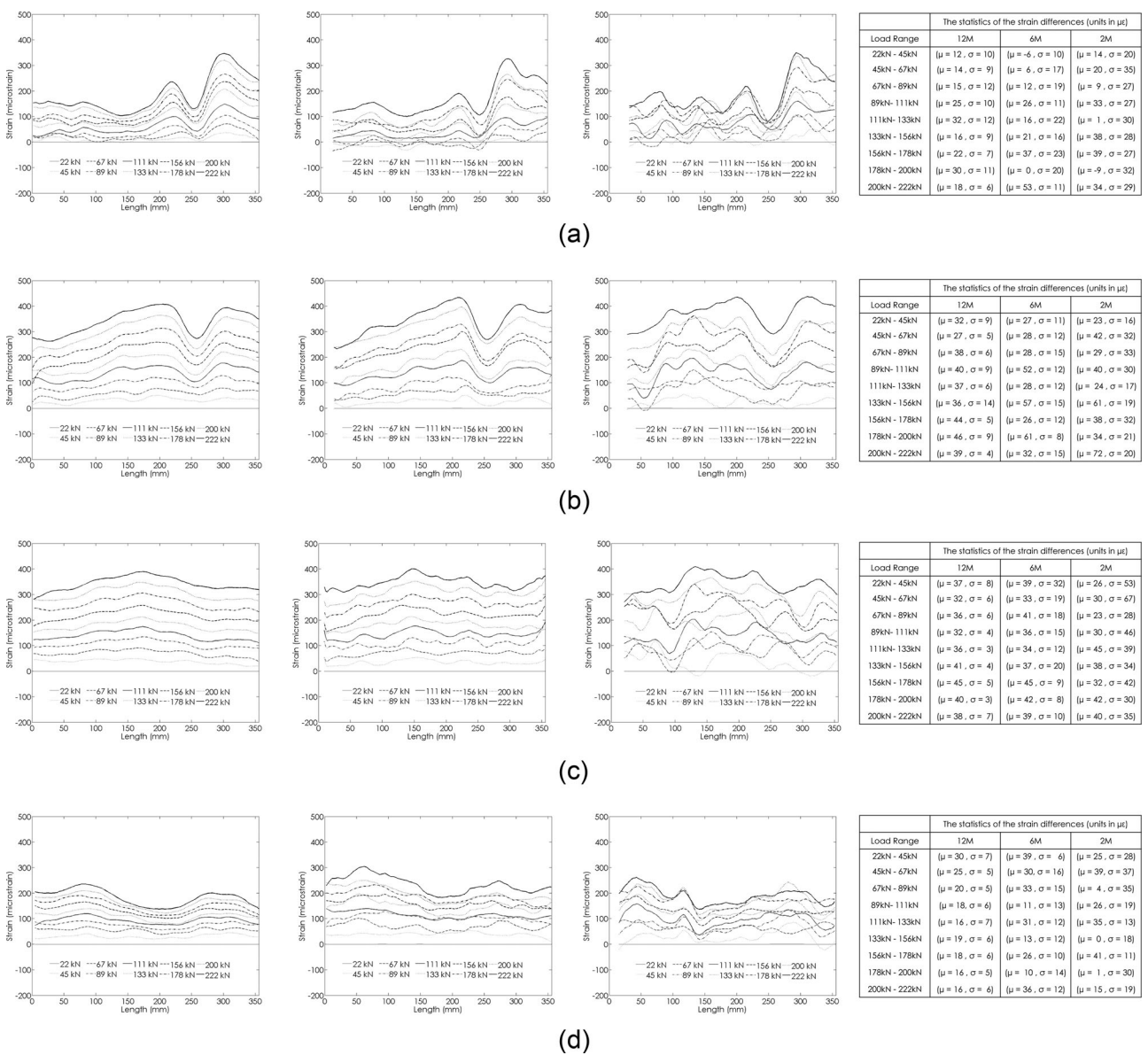


Figure 9. Strain values of the cross sections for the first damage scenario. From top to bottom: Plane Y = 469 mm - Plane Y = 393 mm - Plane Y = 317 mm -Plane Y = 241 mm. From left to right: 12 M - 6 M - 2.3 M resolutions - The characterisation of the strain differences.

size of $28 \times 56 \times 1$ are obtained. These strain fields from three DIC systems which are normalised by its absolute maximum are tested by the trained architecture presented in Figure 1. Detection accuracy is defined as the correct prediction of a sample being damaged or healthy. The detection performance of the network for both damage scenarios is computed as 100% (Table 2). In other words, all 2000 samples per DIC system and damage scenario are correctly identified. It is worthwhile to mention that high detection accuracy is accomplished, although there were strain gradients caused by other imperfections rather than the crack. High-stress concentrations are also observable near the welds. The detection performances of the other studies using strain based inputs are provided in Gulgec et al. (2019a).

6.2. Localisation results

Further analysis is achieved by performing the localisation task since the data from healthy samples are not available.

In this task, the localisation marked as correct localisation if the following criteria are satisfied with the pre-defined threshold values:

$$\left| \min(a_1, a_2) - \min(\hat{a}_1, \hat{a}_2) \right| \le \mathsf{thr} \tag{1}$$

$$|\min(b_1, b_2) - \min(\hat{b}_1, \hat{b}_2)| \le \text{thr}$$
 (2)

$$|\max(\hat{a}_1, \hat{a}_2) - \max(a_1, a_2)| \le \text{thr}$$
 (3)

$$|\max(\hat{b}_1, \hat{b}_2) - \max(b_1, b_2)| \le \mathsf{thr}$$
 (4)

 $(\hat{a}_1, \hat{a}_2, \hat{b}_1, \hat{b}_2)$ are predicted box coordinates, (a_1, a_2, b_1, b_2) are true box coordinates, and thr is the userdefined threshold.

Three different thresholds are adopted, thr $= 13 \, \text{mm}$, thr $= 25 \,\mathrm{mm}$ and thr $= 51 \,\mathrm{mm}$, to assess the accuracy of the method with three different DIC systems. Figure 19 visualises the localisation accuracy results for the first damage scenario. According to the figure, the proposed architecture localises the crack with 100% accuracy when the threshold value is 13 mm and the load is greater than 133 kN when

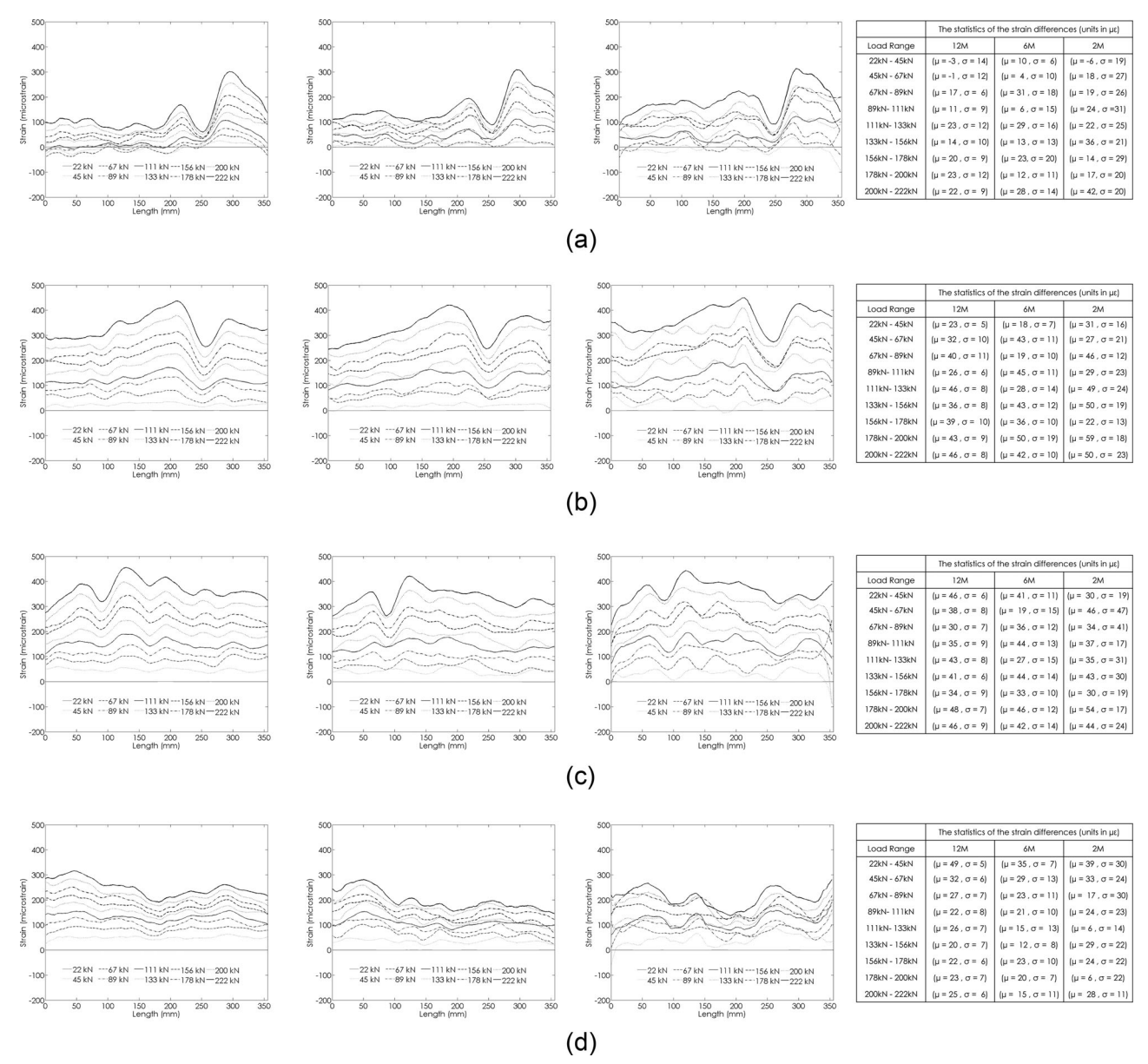


Figure 10. Strain values of the cross sections for the second damage scenario. From top to bottom: Plane $Y = 469 \, \text{mm} - \text{Plane} \ Y = 393 \, \text{mm} - \text{Plane} \ Y = 317 \, \text{mm} - \text{Plane} \ Y = 241 \, \text{mm}$. From left to right: $12 \, \text{M} - 6 \, \text{M} - 2.3 \, \text{M}$ resolutions – The characterisation of the strain differences.

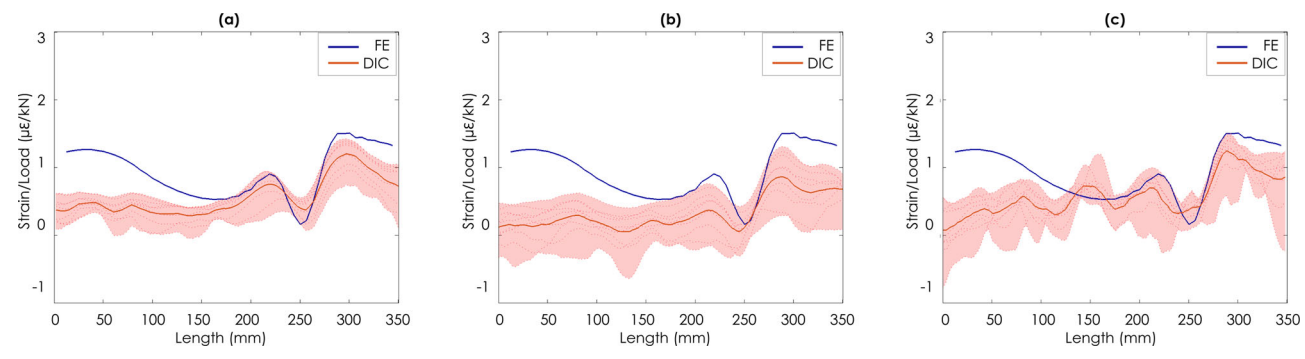


Figure 11. Strain values of the cross section at plane Y = 469 mm for the cameras with the resolution of (a) 12 M, (b) 6 M, (c) 2.3 M.

the high-resolution camera system (i.e. $12\,\mathrm{M}$) is used. Although the accuracy seems to decrease for the small loads for thr = $13\,\mathrm{mm}$, the accuracy reaches 80% when the crack location is searched in the broader area by increasing the threshold. With the increase in the threshold, the

localisation accuracy increases. Figure 19 also shows that the reduction in the camera resolution results in lower accuracy in the localisation task.

A similar analysis for each load level is also performed on the second crack scenario to assess the evolving nature

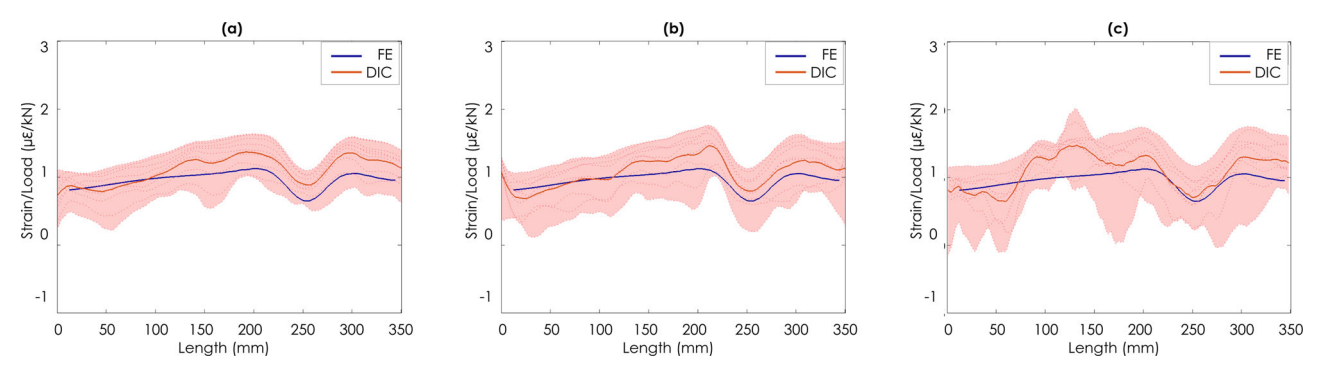


Figure 12. Strain values of the cross section at plane Y = 393 mm for the cameras with the resolution of (a) 12 M, (b) 6 M, (c) 2.3 M.

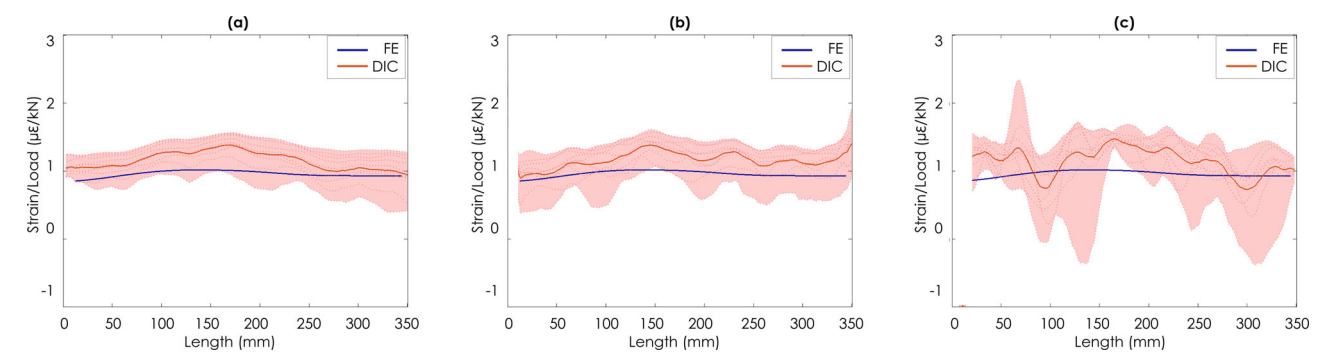


Figure 13. Strain values of the cross section at plane Y = 317 mm for the cameras with the resolution of (a) 12 M, (b) 6 M, (c) 2.3 M.

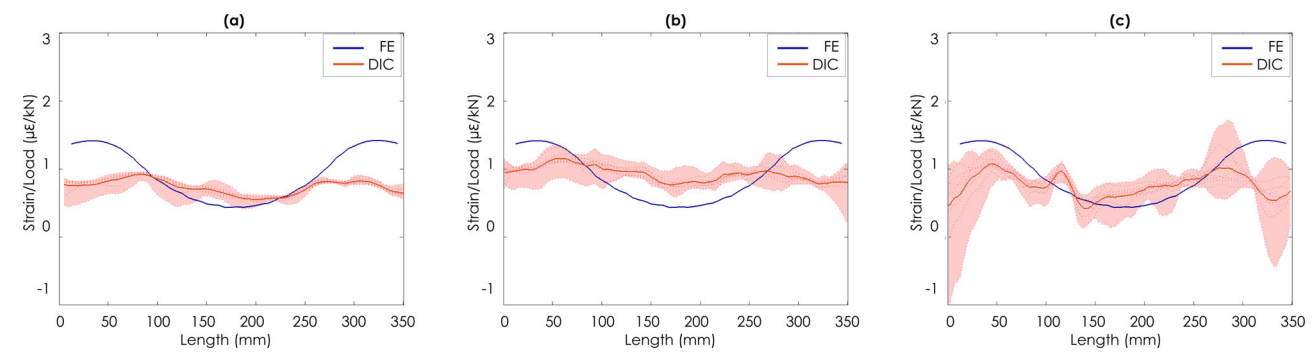


Figure 14. Strain values of the cross section at plane Y = 241 mm for the cameras with the resolution of (a) 12 M, (b) 6 M, (c) 2.3 M.

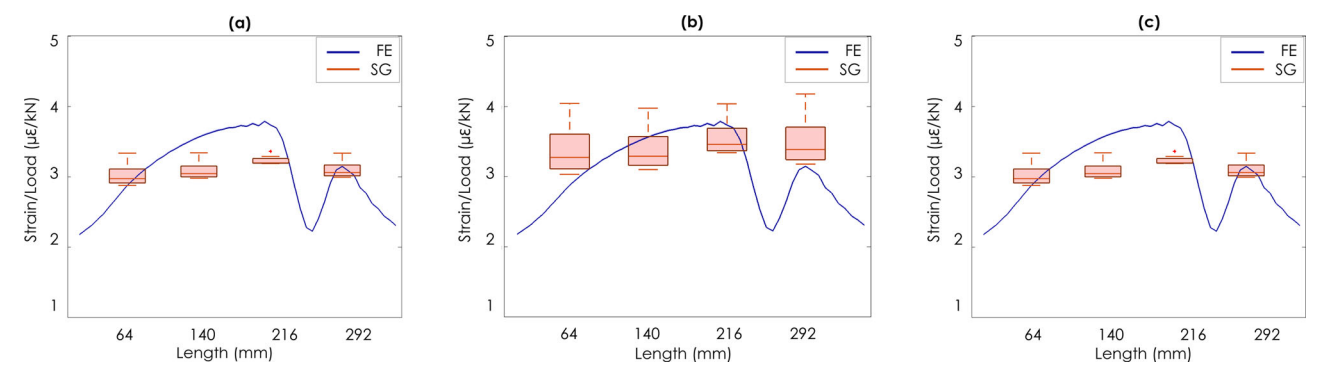


Figure 15. Strain values of the cross section at plane Y = 469 mm for the experiment where (a) 12 M, (b) 6 M, (c) 2.3 M are utilised.

of the crack case. For each strain field, the first crack case is defined as a baseline condition and subtracted from the strain field in the second crack scenario. The mean and the minimum of these fields are computed. The input is normalised by subtracting the mean and adding the minimum before feeding the trained network architecture.

Figure 20 shows the localisation accuracy results for the second damage scenario. According to the figure, it can be seen that the localisation result decreases for the second crack location for the threshold value of 13 mm. With the increase in the threshold value, higher accuracy for all load levels is obtained for the high-resolution DIC system.

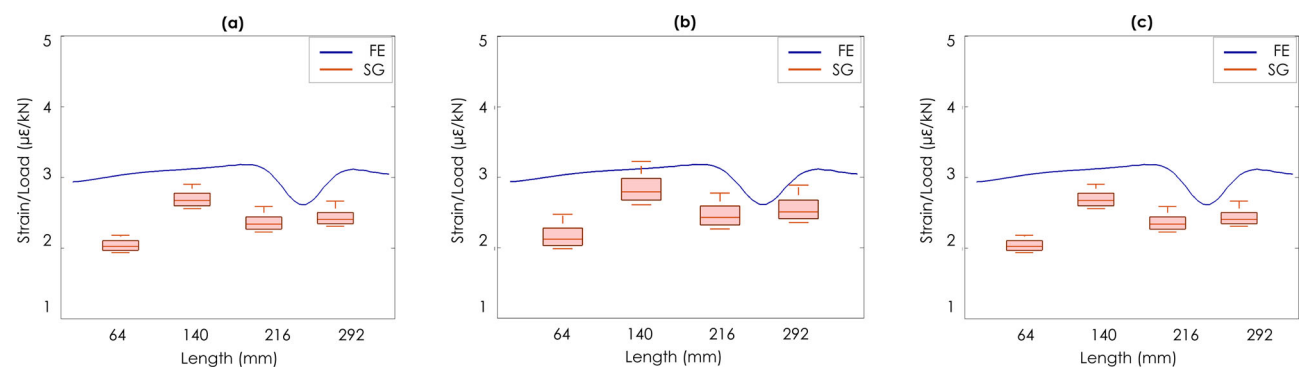


Figure 16. Strain values of the cross section at plane Y = 393 mm for the experiment where (a) 12 M, (b) 6 M, (c) 2.3 M are utilised.

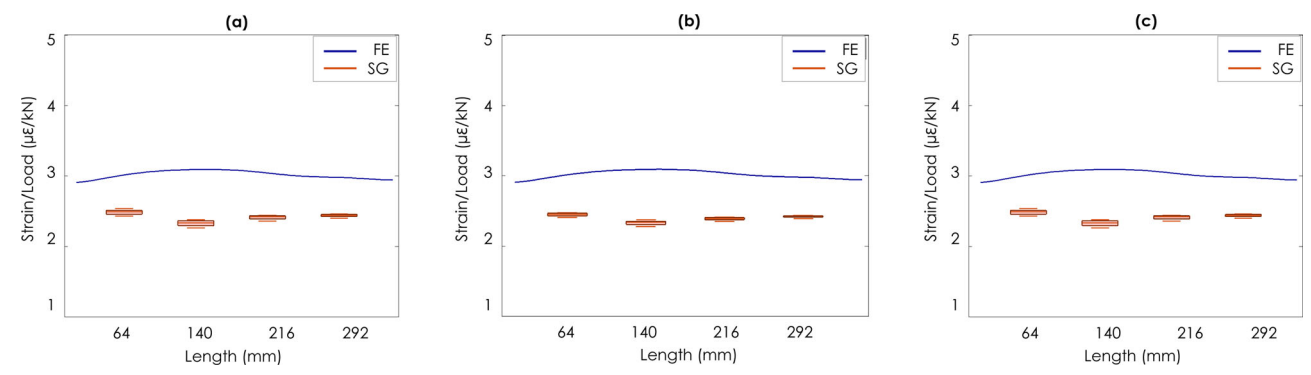


Figure 17. Strain values of the cross section at plane Y = 317 mm for the experiment where (a) 12 M, (b) 6 M, (c) 2.3 M are utilised.

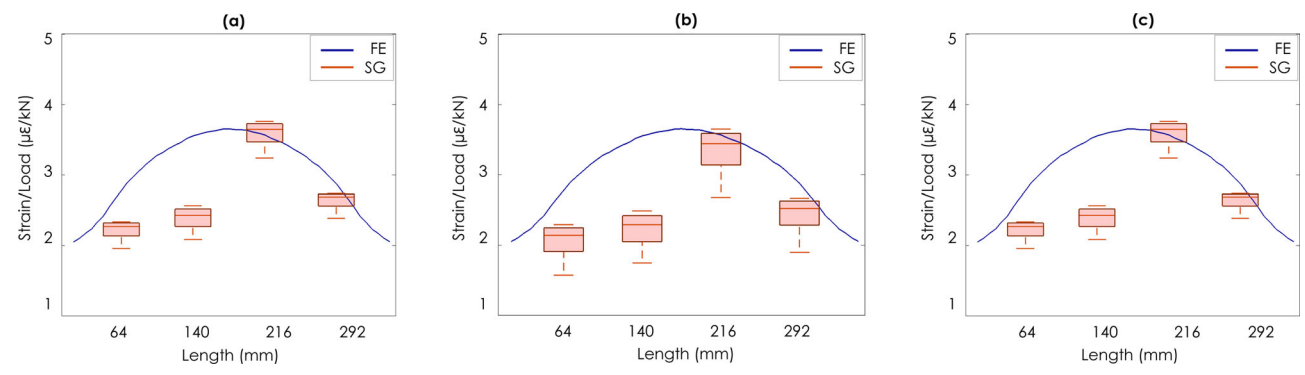


Figure 18. Strain values of the cross section at plane Y = 241 mm for the experiment where (a) 12 M, (b) 6 M, (c) 2.3 M are utilised.

Table 2. Detection performance of the network.

			Load (kN)								
		45	67	89	111	133	156	178	200	222	
First crack	2M	100%	100%	100%	100%	100%	100%	100%	100%	100%	
	6M	100%	100%	100%	100%	100%	100%	100%	100%	100%	
	12M	100%	100%	100%	100%	100%	100%	100%	100%	100%	
Second crack	2M	100%	100%	100%	100%	100%	100%	100%	100%	100%	
	6M	100%	100%	100%	100%	100%	100%	100%	100%	100%	
	12M	100%	100%	100%	100%	100%	100%	100%	100%	100%	

Nevertheless, using 2.3 M and 6 M does not provide high accuracy in smaller load levels.

7. Conclusions

The laboratory testing of a steel structural connection was conducted by using Digital Image Correlation to address two main scopes of the article: (i) exploring whether small strain responses are achievable with the current DIC

systems, (ii) validating previously proposed real-time damage diagnosis platform on the collected data.

To address the first purpose, strain responses of the specimen were measured via strain gauge and three different DIC systems with three camera resolutions. The measured small strain responses of the steel component using different DIC systems were discussed and verified against those measured by strain gauge and the finite element method. The findings of this article indicate that DIC measures small

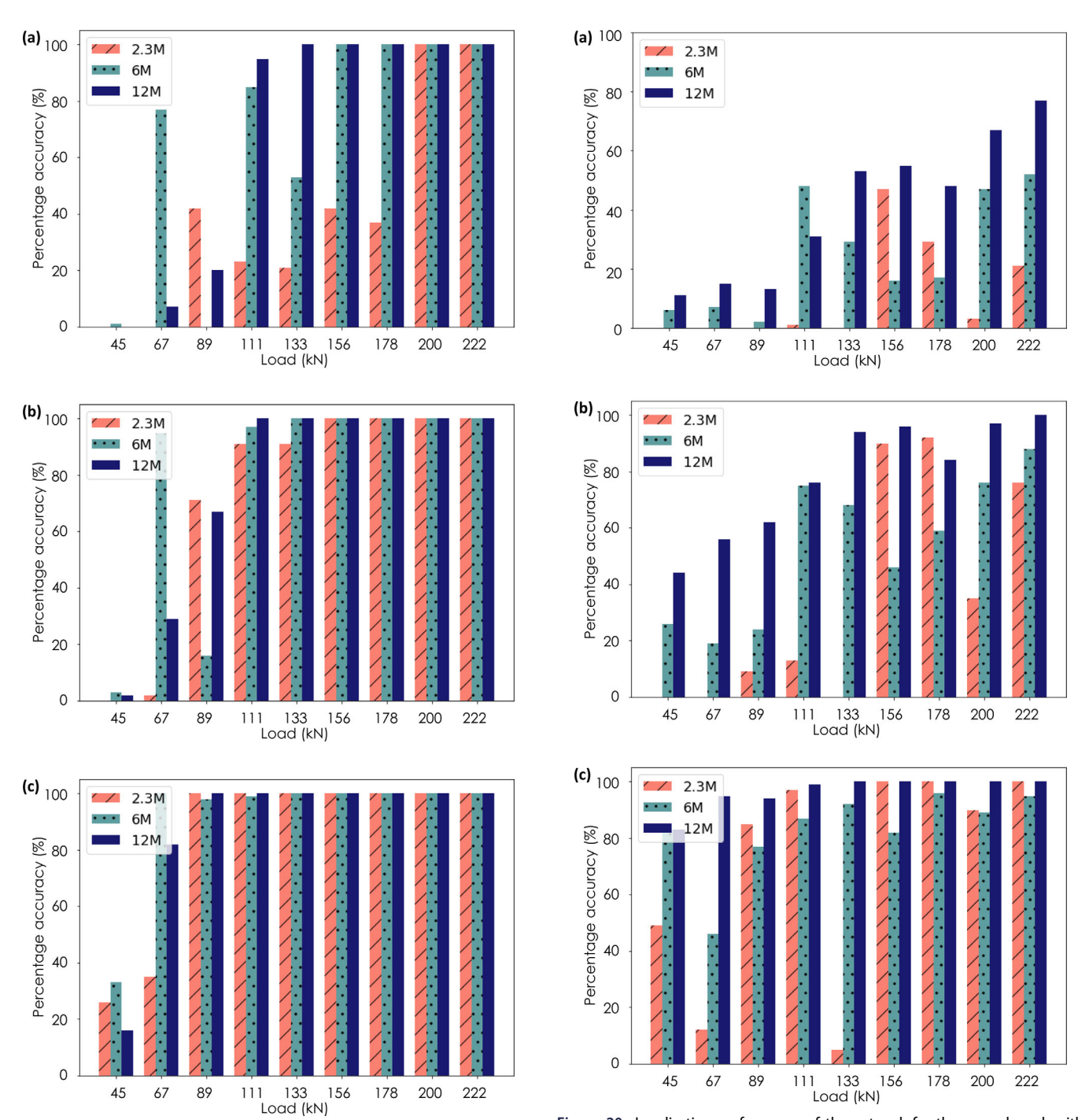


Figure 19. Localisation performance of the network for the first crack with threshold values of (a) 13 mm, (b) 25 mm, (c) 51 mm.

Figure 20. Localisation performance of the network for the second crack with threshold values of (a) 13 mm, (b) 25 mm, (c) 51 mm.

strains of the large-scale specimens only with high-resolution cameras and under highly controlled laboratory conditions. Increasing the accuracy of DIC, especially for field testing conditions, is still ongoing research in SHM community.

As a second purpose, the performance and efficiency of damage detection and localisation approach were evaluated on two induced damage conditions. Deep learning achieves remarkable generalisation when it is designed carefully such that it can perform successfully even with unseen cases. The designed architecture diagnoses damages on samples collected by DIC with high accuracy, although training dataset

only includes finite element simulations. Moreover, this generalisation is observable for the localisation task. The location of the crack was predicted successfully, although the crack location was not given as input during training.

Digital image correlation is a promising sensing method to overcome the limitations of strain gauges since it first and foremost eliminates the installation costs associated with fixed sensor networks, and in some cases may be the only option if specific fixed sensors were not installed prior to construction. DIC can also be utilised to automatise the real-time structural damage diagnosis as discussed throughout the manuscript.



Disclosure statement

No potential conflict of interest was reported by the authors.

Funding

Research funding is partially provided by the National Science Foundation through Grant No. CMMI-1351537 by Hazard Mitigation and Structural Engineering program, and by a grant from the Commonwealth of Pennsylvania, Department of Community and Economic Development, through the Pennsylvania Infrastructure Technology Alliance (PITA). Martin Takáč was supported by National Science Foundation grants CCF-1618717, CMMI-1663256 and NSF:CCF:1740796.

References

- Acciaioli, A., Lionello, G., & Baleani, M. (2018). Experimentally achievable accuracy using a digital image correlation technique in measuring small-magnitude (<0.1%) homogeneous strain fields. Materials, 11(5), 751. doi:10.3390/ma11050751
- Alampalli, S., & Lund, R. (2006). Estimating fatigue life of bridge components using measured strains. Journal of Bridge Engineering, 11(6), 725-736. doi:10.1061/(ASCE)1084-0702(2006)11:6(725)
- Amiot, F., Bornert, M., Doumalin, P., Dupré, J.-C., Fazzini, M., Orteu, J.-J., Poilâne, C., Robert, L., Rotinat, R., Toussaint, E., Wattrisse, B., & Wienin, J. S. (2013). Assessment of digital image correlation measurement accuracy in the ultimate error regime: Main results of a collaborative benchmark. Strain, 49(6), 483-496. doi:10.1111/str.
- Berfield, T., Patel, J., Shimmin, R., Braun, P., Lambros, J., & Sottos, N. (2007). Micro-and nanoscale deformation measurement of surface and internal planes via digital image correlation. Experimental Mechanics, 47(1), 51-62. doi:10.1007/s11340-006-0531-2
- Bing, P., Hui-Min, X., Bo-Qin, X., & Fu-Long, D. (2006). Performance of sub-pixel registration algorithms in digital image correlation. Measurement Science and Technology, 17(6), 1615-1621. doi:10. 1088/0957-0233/17/6/045
- Bornert, M., Brémand, F., Doumalin, P., Dupré, J.-C., Fazzini, M., Grédiac, M., Hild, F., Mistou, S., Molimard, J., Orteu, J.-J., Robert, L., Surrel, Y., Vacher, P., & Wattrisse, B. (2009). Assessment of digital image correlation measurement errors: Methodology and results. Experimental Mechanics, 49(3), 353-370. doi:10.1007/s11340-008-9204-7
- Chu, T., Ranson, W., & Sutton, M. A. (1985). Applications of digitalimage-correlation techniques to experimental Experimental Mechanics, 25(3), 232-244. doi:10.1007/BF02325092
- Crammond, G., Boyd, S., & Dulieu-Barton, J. (2013). Speckle pattern quality assessment for digital image correlation. Optics and Lasers in Engineering, 51(12), 1368-1378. doi:10.1016/j.optlaseng.2013.03.014
- Desai, N. (2016). Small-strain measurement in bridge connections using the Digital Image Correlation (DIC) technique. In Health Monitoring of Structural and Biological Systems 2016 (Vol. 9805, p. 980530). doi:10.1117/12.2234454
- Dinh, N. V., Hassan, G. M., Dyskin, A. V., & MacNish, C. (2015). Digital image correlation for small strain measurement in deformable solids and geomechanical structures. In 2015 IEEE International Conference on Image Processing (ICIP) (pp. 3324-3328). doi:10. 1109/ICIP.2015.7351419
- Fang, X., Luo, H., & Tang, J. (2005). Structural damage detection using neural network with learning rate improvement. Computers & Structures, 83(25-26), 2150-2161. doi:10.1016/j.compstruc.2005.02.
- Garifullin, M., Bronzova, M., Jokinen, T., Heinisuo, M., & Kovačič, B. (2016). Effect of fillet welds on initial rotational stiffness of welded tubular joints. Procedia Engineering, 165, 1643-1650. doi:10.1016/j. proeng.2016.11.905

- GOM. (2013). ARAMIS user manual-Software. Braunschweig: GOM mbH Braunschweig.
- Grytten, F., Daiyan, H., Polanco-Loria, M., & Dumoulin, S. (2009). Use of digital image correlation to measure large-strain tensile properties of ductile thermoplastics. Polymer Testing, 28(6), 653-660. doi:10. 1016/j.polymertesting.2009.05.009
- Gulgec, N. S., Takáč, M., & Pakzad, S. N. (2017). Structural damage detection using convolutional neural networks. In Barthorpe R., Platz R., Lopez I., Moaveni B., Papadimitriou C. (Eds.). Model validation and uncertainty quantification (Vol. 3, pp. 331-337). Berlin: Springer.
- Gulgec, N. S., Takáč, M., & Pakzad, S. N. (2019a). Convolutional neural network approach for robust structural damage detection and localisation. Journal of Computing in Civil Engineering, 33(3), 04019005. doi:10.1061/(ASCE)CP.1943-5487.0000820
- Gulgec, N. S., Takáč, M., & Pakzad, S. N. (2019b). Innovative sensing by using deep learning framework. In Pakzad S. (Ed.). Dynamics of civil structures (Vol. 2, pp. 293-300). Berlin: Springer.
- Gulgec, N. S., Takáč, M., & Pakzad, S. N. (2020). Experimental study on digital image correlation for deep learning-based damage diagnostic. In Pakzad S. (Ed.). Dynamics of civil structures (Vol. 2, pp. 205-210). Berlin: Springer.
- Haddadi, H., & Belhabib, S. (2008). Use of rigid-body motion for the investigation and estimation of the measurement errors related to digital image correlation technique. Optics and Lasers Engineering, 46(2), 185-196. doi:10.1016/j.optlaseng.2007.05.008
- Hung, P.-C., & Voloshin, A. (2003). In-plane strain measurement by digital image correlation. Journal of the Brazilian Society of Mechanical Sciences and Engineering, 25(3), 215-221. doi:10.1590/ \$1678-58782003000300001
- Hutt, T., & Cawley, P. (2009). Feasibility of digital image correlation for detection of cracks at fastener holes. NDT & E International, 42(2), 141-149. doi:10.1016/j.ndteint.2008.10.008
- Jerabek, M., Major, Z., & Lang, R. W. (2010). Strain determination of polymeric materials using digital image correlation. Polymer Testing, 29(3), 407-416. doi:10.1016/j.polymertesting.2010.01.005
- Jones, I., & Iadicola, M. (2018). A good practices guide for digital image correlation. International Digital Image Correlation Society.
- Kim, S., Pakzad, S., Culler, D., Demmel, J., Fenves, G., & Glaser, S. (2007). Health monitoring of civil infrastructures using wireless sensor networks. In Proceedings of the 6th international conference on Information processing in sensor networks (pp. 254-263). doi:10. 1145/1236360.1236395
- Lagattu, F., Bridier, F., Villechaise, P., & Brillaud, J. (2006). In-plane strain measurements on a microscopic scale by coupling digital image correlation and an in situ SEM technique. Materials Characterization, 56(1), 10-18. doi:10.1016/j.matchar.2005.08.004
- LeBlanc, B., Niezrecki, C., Avitabile, P., Chen, J., & Sherwood, J. (2013). Damage detection and full surface characterization of a wind turbine blade using three-dimensional digital image correlation. Structural Health Monitoring: An International Journal, 12(5-6), 430-439, doi:10.1177/1475921713506766
- Lecompte, D., Smits, A., Bossuyt, S., Sol, H., Vantomme, J., Van Hemelrijck, D., & Habraken, A.M. (2006). Quality assessment of speckle patterns for digital image correlation. Optics and Lasers in Engineering, 44(11), 1132–1145. doi:10.1016/j.optlaseng.2005.10.004
- LeCun, Y., Bottou, L., Bengio, Y., & Haffner, P. (1998). Gradient-based learning applied to document recognition. Proceedings of the IEEE, 86(11), 2278-2324. doi:10.1109/5.726791
- Lee, C., Take, W. A., & Hoult, N. A. (2012). Optimum accuracy of two-dimensional strain measurements using digital image correlation. Journal of Computing in Civil Engineering, 26(6), 795-803. doi:10.1061/(ASCE)CP.1943-5487.0000182
- Ma, S., Pang, J., & Ma, Q. (2012). The systematic error in digital image correlation induced by self-heating of a digital camera. Measurement Science and Technology, 23(2), 025403. doi:10.1088/0957-0233/23/2/
- Mehdi Mirzazadeh, M., & Green, M. F. (2018). Fiber optic sensors and digital image correlation for measuring deformations in reinforced



- concrete beams. Journal of Bridge Engineering, 23(3), 04017144. doi: 10.1061/(ASCE)BE.1943-5592.0001189
- Pan, B. (2018). Digital image correlation for surface deformation measurement: Historical developments, recent advances and future goals. Measurement Science and Technology, 29(8), 082001. doi:10.1088/ 1361-6501/aac55b
- Pan, B., Xie, H., & Wang, Z. (2010). Equivalence of digital image correlation criteria for pattern matching. Applied Optics, 49(28), 5501-5509. doi:10.1364/AO.49.005501
- Pan, B., Xie, H., Wang, Z., Qian, K., & Wang, Z. (2008). Study on subset size selection in digital image correlation for speckle patterns. Optics Express, 16(10), 7037-7048. doi:10.1364/OE.16.007037
- Patterson, E. A., Hack, E., Brailly, P., Burguete, R. L., Saleem, Q., Siebert, T., Tomlinson, R. A., & Whelan, M. P. (2007). Calibration and evaluation of optical systems for full-field strain measurement. Optics and Lasers in Engineering, 45(5), 550-564. doi:10.1016/j.optlaseng.2006.08.012
- Périé, J.-N., Calloch, S., Cluzel, C., & Hild, F. (2002). Analysis of a multiaxial test on a C/C composite by using digital image correlation and a damage model. Experimental Mechanics, 42(3), 318-328. doi:10.1177/001448502321548418
- Pritchard, R. H., Lava, P., Debruyne, D., & Terentjev, E. M. (2013). Precise determination of the poisson ratio in soft materials with 2D digital image correlation. Soft Matter, 9(26), 6037-6045. doi:10.1039/ c3sm50901j
- Reu, P. (2011). Experimental and numerical methods for exact subpixel shifting. Experimental Mechanics, 51(4), 443-452. doi:10.1007/ s11340-010-9417-4
- Reu, P. (2012). Hidden components of DIC: Calibration and shape function-Part 1. Experimental Techniques, 36(2), 3-5. doi:10.1111/j. 1747-1567.2012.00821.x
- Risbet, M., Feissel, P., Roland, T., Brancherie, D., & Roelandt, J.-M. (2010). Digital image correlation technique: Application to early fatigue damage detection in stainless steel. Procedia Engineering, 2(1), 2219-2227. doi:10.1016/j.proeng.2010.03.238
- Schreier, H., Braasch, J. R., & Sutton, M. A. (2000). Systematic errors in digital image correlation caused by intensity interpolation. Optical Engineering, 39(11), 2915. doi:10.1117/1.1314593
- Schreier, H., Orteu, J.-J., & Sutton, M. (2009). Image correlation for shape, motion and deformation measurements: Basic concepts, theory and applications (Vol. 1). New York, NY: Springer.
- Siebert, T., Becker, T., Spiltthof, K., Neumann, I., & Krupka, R. (2007). Error estimations in digital image correlation technique. Applied

- Mechanics and Materials, 7-8, 265-270. doi:10.4028/www.scientific. net/AMM.7-8.265
- Smith, B., Li, X., & Tong, W. (1998). Error assessment for strain mapping by digital image correlation. Experimental Techniques, 22(4), 19-21. doi:10.1111/j.1747-1567.1998.tb02332.x
- Sutton, M., Orteu, J. J., & Schreier, H. (2009). Image correlation for shape, motion and deformation measurements: Basic concepts, theory and applications. Berlin: Springer Science & Business Media.
- Sutton, M., Wolters, W., Peters, W., Ranson, W., & McNeill, S. (1983). Determination of displacements using an improved digital correlation method. Image and Vision Computing, 1(3), 133-139. doi:10. 1016/0262-8856(83)90064-1
- Sutton, M., Yan, J., Tiwari, V., Schreier, H., & Orteu, J.-J. (2008). The effect of out-of-plane motion on 2D and 3D digital image correlation measurements. Optics and Lasers in Engineering, 46(10), 746-757. doi:10.1016/j.optlaseng.2008.05.005
- Tang, Z., Liang, J., Xiao, Z., & Guo, C. (2012). Large deformation measurement scheme for 3D digital image correlation method. Optics and Lasers in Engineering, 50(2), 122-130. doi:10.1016/j.optlaseng.2011.09.018
- Tennyson, R., Mufti, A., Rizkalla, S., Tadros, G., & Benmokrane, B. (2001). Structural health monitoring of innovative bridges in Canada with fiber optic sensors. Smart Materials and Structures, 10(3), 560-573. doi:10.1088/0964-1726/10/3/320
- Wang, Y. H., Jiang, J. H., Wanintrudal, C., Du, C., Zhou, D., Smith, L. M., & Yang, L. X. (2010). Whole field sheet-metal tensile test using digital image correlation. Experimental Techniques, 34(2), 54-59. doi:10.1111/j.1747-1567.2009.00483.x
- Wattrisse, B., Chrysochoos, A., Muracciole, J.-M., & Némoz-Gaillard, M. (2001). Analysis of strain localisation during tensile tests by digital image correlation. Experimental Mechanics, 41(1), 29-39. doi: 10.1007/BF02323101
- Yaofeng, S., & Pang, J. H. (2007). Study of optimal subset size in digital image correlation of speckle pattern images. Optics and Lasers in Engineering, 45(9), 967-974. doi:10.1016/j.optlaseng.2007. 01.012
- Yoneyama, S., Kikuta, H., Kitagawa, A., & Kitamura, K. (2006). Lens distortion correction for digital image correlation by measuring rigid body displacement. Optical Engineering, 45(2), 023602. doi:10. 1117/1.2168411
- Zhang, D. S., Luo, M., & Arola, D. D. (2006). Displacement/strain measurements using an optical microscope and digital image correlation. Optical Engineering, 45(3), 033605. doi:10.1117/1.2182108